

Article

Production of a Non-Stoichiometric Nb-Ti HSLA Steel by Thermomechanical Processing on a Steckel Mill

Cleiton Arlindo Martins ^{1,*}, Geraldo Lúcio de Faria ², Unai Mayo ^{3,4}, Nerea Isasti ^{3,4}, Pello Uranga ^{3,4}, Jose Maria Rodríguez-Ibabe ^{3,4}, Altair Lúcio de Souza ⁵, Jorge Adam Cleto Cohn ⁵, Marcelo Arantes Rebellato ⁶ and Antônio Augusto Gorni ⁶

¹ Gerdau Ouro Branco, Rolling Mill, Ouro Branco 36420-000, Minas Gerais, Brazil

² Metallurgical and Materials Engineering Department (DEMET), Escola de Minas, Universidade Federal de Ouro Preto, Ouro Preto 35400-000, Minas Gerais, Brazil

³ CEIT-Basque Research and Technology Alliance (BRTA), Materials and Manufacturing Division, 20018 Donostia-San Sebastián, Basque Country, Spain

⁴ Mechanical and Materials Engineering Department, Universidad de Navarra, Tecnun, 20018 Donostia-San Sebastián, Basque Country, Spain

⁵ Gerdau Ouro Branco, Research and Development, Ouro Branco 36420-000, Minas Gerais, Brazil

⁶ Companhia Brasileira de Mineração e Metalurgia, CBMM, Araxá 04538-133, Minas Gerais, Brazil

* Correspondence: cleiton.martins@gerdau.com.br

Abstract: Obtaining high levels of mechanical properties in steels is directly linked to the use of special mechanical forming processes and the addition of alloying elements during their manufacture. This work presents a study of a hot-rolled steel strip produced to achieve a yield strength above 600 MPa, using a niobium microalloyed HSLA steel with non-stoichiometric titanium (titanium/nitrogen ratio above 3.42), and rolled on a Steckel mill. A major challenge imposed by rolling on a Steckel mill is that the process is reversible, resulting in long interpass times, which facilitates recrystallization and grain growth kinetics. Rolling parameters whose aim was to obtain the maximum degree of microstructural refinement were determined by considering microstructural evolution simulations performed in MicroSim-SM[®] software and studying the alloy through physical simulations to obtain critical temperatures and determine the CCT diagram. Four ranges of coiling temperatures (525–550 °C/550–600 °C/600–650 °C/650–700 °C) were applied to evaluate their impact on microstructure, precipitation hardening, and mechanical properties, with the results showing a very refined microstructure, with the highest yield strength observed at coiling temperatures of 600–650 °C. This scenario is explained by the maximum precipitation of titanium carbide observed at this temperature, leading to a greater contribution of precipitation hardening provided by the presence of a large volume of small-sized precipitates. This paper shows that the combination of optimized industrial parameters based on metallurgical mechanisms and advanced modeling techniques opens up new possibilities for a robust production of high-strength steels using a Steckel mill. The microstructural base for a stable production of high-strength hot-rolled products relies on a consistent grain size refinement provided mainly by the effect of Nb together with appropriate rolling parameters, and the fine precipitation of TiC during cooling provides the additional increase to reach the requested yield strength values.

Keywords: controlled rolling; thermomechanical processing; accelerated cooling; high-strength low-alloy steels; Nb precipitation; TiC precipitation; Steckel mill; non-stoichiometric alloy



Citation: Martins, C.A.; de Faria, G.L.; Mayo, U.; Isasti, N.; Uranga, P.; Rodríguez-Ibabe, J.M.; de Souza, A.L.; Cohn, J.A.C.; Rebellato, M.A.; Gorni, A.A. Production of a Non-Stoichiometric Nb-Ti HSLA Steel by Thermomechanical Processing on a Steckel Mill. *Metals* **2023**, *13*, 405. <https://doi.org/10.3390/met13020405>

Academic Editor: João Pedro Oliveira

Received: 12 January 2023

Revised: 31 January 2023

Accepted: 10 February 2023

Published: 16 February 2023



Copyright: © 2023 by the authors. Licensee MDPI, Basel, Switzerland. This article is an open access article distributed under the terms and conditions of the Creative Commons Attribution (CC BY) license (<https://creativecommons.org/licenses/by/4.0/>).

1. Introduction

High-Strength Low-Alloy (HSLA) steels are widely used in applications where high yield strength (YS) and tensile strength (TS) are demanded [1–5]. Load-lifting structures are examples of applications that require a yield strength above 600 MPa. In this context, HSLA steels gain relevance due to their low carbon content that improves weldability and

formability. The lower levels of mechanical properties that result from decreased carbon contents can be counterbalanced by the addition of alloying elements such as niobium (Nb) and titanium (Ti), and an appropriate thermomechanical process [6–10].

Recently, special attention has been paid to the significant precipitation hardening obtained by addition of high Ti levels (higher than 0.05 wt%) in low-carbon steels, due to the formation of a high density of ultrafine precipitates during or after phase transformation [9,11]. Commonly, high Ti is added in combination with other microalloying elements, such as Mo [12,13], V [14], or Nb [15–17]. Among the different alloy concepts, the most investigated one is Ti-Mo steel grade. Several works claim [18,19] that addition of Mo results in a refinement of the precipitates formed during phase transformation, ensuring higher fine precipitation strengthening.

The additions of Nb and Ti help the final product to develop a ferrite-pearlite microstructure with a high level of refinement and, in addition, allow considerable precipitation hardening [20]. When associated with the controlled rolling process, the addition of 0.030% to 0.060 wt% Nb has the ability to reduce the temperature range in which recrystallization occurs between rolling passes, resulting in a refined and homogeneous microstructure at the rolling end [21–25]. Nb can also provide some hardenability, promoting the formation of non-equilibrium phases [26]. Depending on the Ti and N relation, the role of titanium can be completely different. For low Ti additions (hypostoichiometric Ti), titanium can contribute to microstructural refinement by inhibiting austenite grain growth during hot deformation related to the pinning effect exerted by Ti (C,N) precipitates [27–29]. In this case, before phase transformation, there is no Ti in solid solution. However, for high Ti additions (hyperstoichiometric Ti), the Ti remaining in solid solution prior to transformation can precipitate as very fine TiC (finer than 10 nm) during cooling, promoting a significant precipitation hardening. The main contribution of Ti in terms of strengthening is based on the Orowan mechanism via the formation of TiC nanoprecipitates during the final cooling strategy (run-out table and coiling) [30–34]. According to Elderman and Wigman [35], a yield strength above 600 MPa in HSLA steels is directly associated with an effective titanium value above 0.06 wt%, calculated using Equation (1). Recent studies have shown that another important prerequisite is the Ti/N ratio present in HSLA steels, which must be kept above the stoichiometric value— $Ti/N > 3.42$ [36]. Thus, from the appropriate chemical composition and forming process, it is possible to obtain high levels of mechanical properties, thus eliminating the cost associated with subsequent product heat treatments, retaining low carbon levels in the material and, consequently, improving formability and weldability.

$$Ti_{\text{eff}} \% = Ti_{\text{total}} \% - (3.4 \times N \%) - (1.5 \times S \%) \quad (1)$$

This paper describes the production of a HSLA steel in a thermomechanical rolling route, microalloyed with Nb and Ti, with the titanium addition above the stoichiometric ratio with nitrogen ($Ti/N > 3.4$), with a view to obtaining a minimum yield strength of 600 MPa and minimum tensile strength of 680 MPa. When high Ti levels are added (above the stoichiometric ratio), considerable variability in fine precipitation strengthening occurs, resulting in a large dispersion in tensile properties [1]. Industrially large strength differences can be found from coil to coil, as well as along the strip length and width, due to the instability of the formation of Ti carbides during cooling. TiC precipitation (size and density of precipitates) seems to be very sensitive to small variations in strain, coiling temperature, and cooling profile. The optimum coiling strategy may depend on the alloy-design, rolling parameters and cooling conditions. Therefore, to meet the increasing material demands in terms of tensile properties, for the current Nb-Ti hyperstoichiometric steel, the definition of an optimum coiling temperature window becomes crucial.

Steckel mill rolling presents some singularities when compared to continuous conventional hot strip mills as well as reversible plate mills. The main differences can be defined in the finishing stands. The Steckel mill applies reversal passes with longer interstand times and with much more limited temperature drops between passes due to the two

coiler furnaces located at each side of the roll. The rolling process in the finishing step is usually conducted by applying tension between the mandrel of the input and output furnaces, called the drum, with the rolling mill to ensure the strip alignment during the rolling process. Depending on the applied tension, stretching in the strip can occur, causing a loss in the strip width. This tension is continuously controlled by the mill, minimizing product width deviations. The tensional status of the strip does not imply any metallurgical effect in the material [37]. The process design that offered microstructural refinement to the final product was modeled by MicroSim-SM[®], a software capable of simulating the microstructural evolution of austenite during rolling using equations that are based on the grain size distribution evolution of austenite and on forming process parameters [38]. The non-recrystallization temperature of the alloy was experimentally obtained by hot torsion tests, while phase transformation was also analyzed using dilatometry tests and CCT diagrams were determined under different austenite conditions (recrystallized and pancaked). Strips were produced in Gerdau Ouro Branco's Steckel mill and four different coiling temperature ranges (525–550 °C/550–600 °C/600–650 °C/650–700 °C) were used in order to identify the best condition under which to obtain the greatest precipitation hardening contribution encouraged by the presence of TiC. Recent studies have shown that, in the case of similar alloys, the coiling temperature that potentiates the largest volume of TiC precipitation is within the range of 600–650 °C [39].

Mechanical properties were measured in tensile tests and the contribution made by the different strengthening mechanisms, such as grain size refinement, secondary phases, precipitation hardening, solid solution, and dislocation strengthening, were calculated using quantitative data from microstructural characterization and predictability equations available in the literature [4,40–42]. A detailed characterization of the microstructure is described using mainly the electron backscattered diffraction technique (EBSD), as well as transmission electron microscopy (TEM).

2. Materials and Methods

The chemical composition of the alloy was a HSLA low carbon, microalloyed with Nb (0.056 wt%) and hyperstoichiometric Ti (0.101 wt%), with composition ranges shown in Table 1.

Table 1. Chemical composition of the alloy subject to study (in weight %).

C	Mn	Nb	Ti	N
0.08–0.1	1.40–1.60	0.05–0.06	0.08–0.12	<0.007

The effective titanium value, calculated based on Equation (1), was 0.07%, and the Ti/N ratio was approximately 16, above the stoichiometric value of 3.42.

Multipass torsion tests were performed to determine the non-recrystallization temperature (T_{nr}). Before deformation, the specimens were preheated for 15 min at 1180 °C, and were then deformed in multipass torsion tests performed at decreasing temperature in the range of 1150–670 °C. The decrease in temperature between passes was 20 °C, while a constant strain per pass (ϵ) of 0.2 and strain rate of 3 s^{−1} were applied, with the interpass time (t_{ip}) being 10 s. The geometry of torsion specimens took the form of a reduced central gauge section, 15.5 mm in length and 7.5 mm in diameter.

To determine the CCT diagram, different thermomechanical cycles were applied in a Bähr 805D deformation dilatometer, as shown in Figure 1, and cylindrical specimens of 10 mm in length and 5 mm in diameter were machined. The dilatometry specimens were reheated at 1180 °C for 15 min and quenched to ensure a full solution of microalloying elements, especially Nb. After further austenitization at 1080 °C for 5 min, a true strain of 0.3 at a constant rate of 1 s^{−1} was then applied. This first deformation pass was performed with the purpose of ensuring a fine recrystallized austenitic structure. In Cycle A, the samples were cooled down slowly to 900 °C, followed by controlled cooling at constant rates in the range between 5 °C/s and 100 °C/s (5, 10, 20, 25, 30, 35, 40, 60, 80, and

100 °C/s). In Cycle B, a second deformation pass of 0.4 ($\epsilon_{acc} = 0.4$) was applied at 900 °C in the non-recrystallization region (below T_{nr}), in order to accumulate strain in the austenite prior to transformation. In Cycle C, the austenite strain accumulation was intensified before transformation by applying two strain passes below T_{nr} ($\epsilon_{acc} = 0.8$), and following the last deformation, the samples were then cooled down at 5, 10, 20, 25, 30, 35, 40, 60, 80, and 100 °C/s to room temperature. From the dilatometry tests, dilation curves were obtained, as well as the evolution of the transformed fraction as a function of temperature, and transformation starting and finishing temperatures were determined as 5 and 95% transformed fractions, respectively. The lever rule was used for calculating the evolution of the transformed fraction from dilation curves. This rule involves extrapolating linear expansion behavior from the temperature regions where no transformation occurs, and subsequently assuming proportionality between the fraction of decomposed austenite and the change in length observed [43–45].

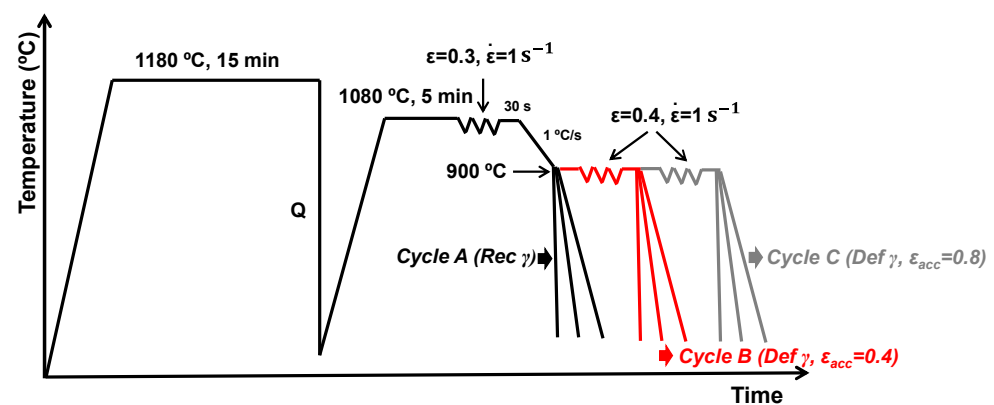


Figure 1. Thermomechanical cycle performed to determine the CCT diagram.

Microstructural evolution simulations of the alloy during the rolling process were performed using the MicroSim-SM[®] model customized for Steckel mill rolling conditions, with the characteristics of austenitic microstructure evolution for each rolling pass being predicted by the model. These calculations are based on metallurgical mechanisms (recrystallization, grain growth, and strain-induced precipitation), which are modeled by equations that consider grain size distribution of the austenitic grains, and on the parameters of the rolling process [46].

Results obtained in the physical and computer simulations allow process parameters to be determined that maximize microstructural refinement of the final product, and, consequently, encourage the hardening mechanism by grain refining.

The strips were produced using thermomechanical processing (controlled rolling) followed by accelerated cooling in an industrial Steckel mill, while the coils were cooled at four different coiling temperature ranges: (525–550 °C/550–600 °C/600–650 °C/650–700 °C), referred to as Sample 1, Sample 2, Sample 3, and Sample 4, respectively. Representative samples were taken from the strips transversely to rolling direction, and tensile tests were carried out in accordance with the ABNT NBR 6673 standard [47]. The total length of the specimen was 480 mm, with a thickness of 8.00 mm. The effective testing length (l_0) was approximately 71.5 mm.

An evaluation of the ferritic grain size distribution was carried out using SEM—EBSD. In order to prepare EBSD specimens, the samples were polished down to 1 μm , with final polishing being undertaken using a 50 nm colloidal silica suspension. Orientation imaging microscopy was carried out on the Philips XL 30CP SEM with a W-filament, using TSL (TexSEM Laboratories, Salt Lake City, UT, USA) equipment, and EBSD mapping performed using a step size of 0.6 μm and accelerating voltage of 20 kV, over a total scanned area of 200 $\mu\text{m} \times 200 \mu\text{m}$. In the current analysis, the minimum pixel per grain was defined as 3 pixels. According to Wilkinson [48], the angular resolution of the EBSD technique is

approximately 0.5° . The scans were then analyzed using TSL OIM™ Analysis 5.31 software (TSL OIM Analysis 5.31 software (EDAX, Mahwah, NJ, USA)).

Precipitation analysis was carried out using a Transmission Electron Microscope (TEM, JEOL 2100, JEOL Ltd., Tokyo, Japan) with a 200 kV voltage and LaB₆ thermionic filament. To characterize precipitation, carbon extraction replicas were employed, and nickel grids were used to support these. Mean precipitate diameters were reported as an average of over 200 measurements and precipitates with diameters smaller than 10 nm were also considered. A total of 15 fields (over $4000 \times 4000 \text{ nm}^2$) were also measured to quantify precipitate size under each condition.

3. Results and Discussion

3.1. Determining the T_{nr} and CCT Diagram

Figure 2a shows the stress–strain curves measured using the multipass torsion test. The Mean Flow Stress (MFS), defined as the area under the stress–strain curve divided by the pass strain [49], was calculated for each deformation pass by numerical integration and plotted as a function of temperature in Figure 2b. Three different regions can be distinguished in these figures: Region I, where complete recrystallization between passes takes place and the stress increase from pass to pass is only due to the temperature drop; Region II, where strain accumulation in austenite occurs; Region III, where some degree of softening due to austenite-to-ferrite transformation occurs. Following the standard procedure [50], the non-recrystallization temperature (T_{nr}) was determined as the intersection between the regression lines of points corresponding to Regions I and II in Figure 2b, at 992°C . The austenite-to-ferrite phase transformation starting (A_{r3}) and finishing (A_{r1}) temperatures were also determined from MFS data (770°C and 730°C , respectively).

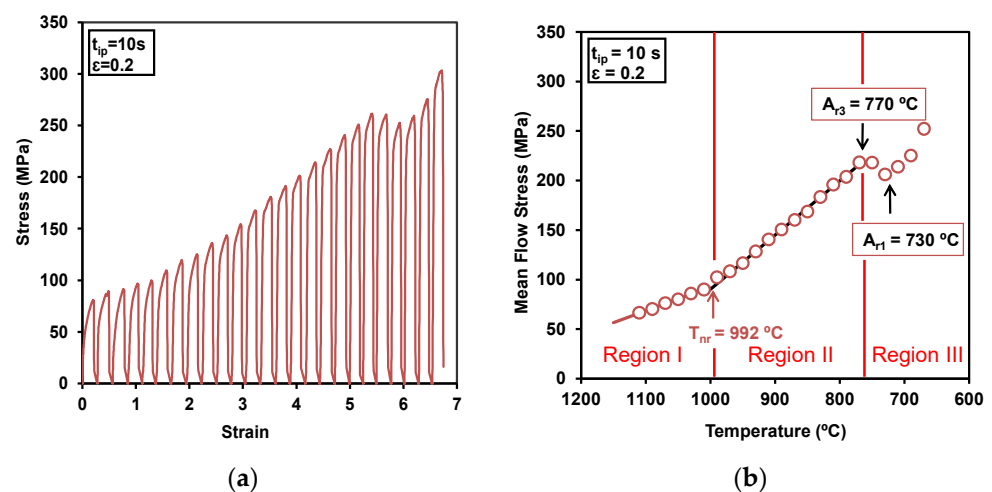


Figure 2. (a) Stress–strain curves obtained using the multipass torsion test ($\epsilon = 0.2$, $t_{ip} = 10 \text{ s}$). (b) Mean flow stress curve versus temperature.

With the aim of plotting the CCT diagram, the sample austenitizing temperature was determined as being 1180°C , which should be sufficient for complete dissolution of the microalloying elements present, according to Irvine [51]. CCT diagrams corresponding to each thermomechanical schedule are shown in Figure 3. Regarding the austenite condition effect, no considerable differences were observed in terms of phase stability regions. In the current paper, the ISIJ Bainite Committee notation has been adopted for naming the different phases [52,53]. In all cases, at the lowest cooling rates of 5 and 10°C/s , the microstructure was composed of polygonal ferrite (PF), degenerated pearlite (DP), and granular ferrite (GF). At cooling rates higher than 30°C/s , more bainitic structures (combinations between quasi-polygonal ferrite (QF) and granular ferrite) can be distinguished, while the formation of bainitic ferrite (BF) was noted at cooling rates higher than 30°C/s .

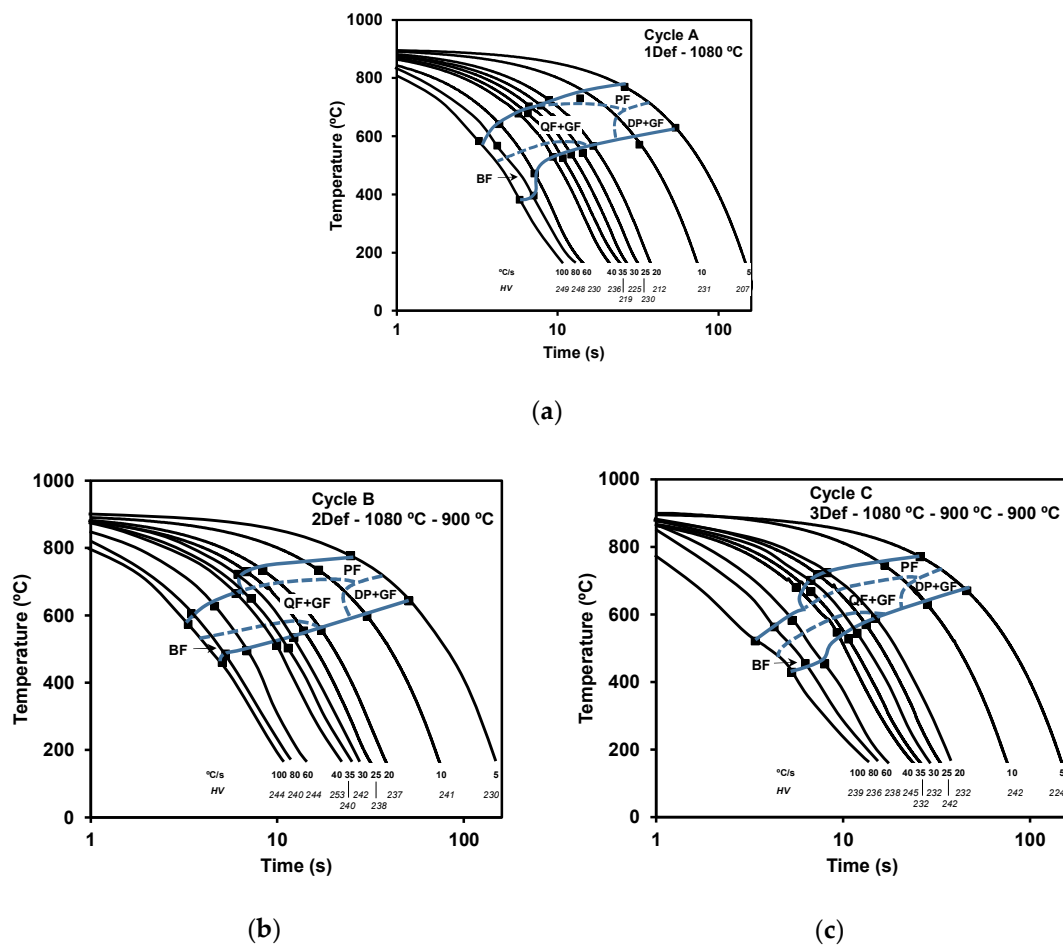


Figure 3. CCT diagrams corresponding to each thermomechanical cycle: (a) Cycle A, (b) Cycle B, and (c) Cycle C. Black lines represent the cooling profile followed at each cooling rate and blue lines determine the stability region of the different phases.

In cycle B, the transformation starting temperatures were slightly higher, especially at cooling rates between 10 and 35 °C/s. The presence of polygonal ferrite can be identified in a large area in the diagram, having been observed even in regions of application of high cooling rates. In comparative terms, while in cycle A (recrystallized austenite), the formation of polygonal ferrite occurred only at cooling rates below 25 °C/s, in cycle B (deformed austenite), the occurrence of polygonal ferrite at rates of up to 35 °C/s was observed. The accumulation of deformed austenite obtained in cycle B encourages an increase in preferential sites of ferrite nucleation [54] and, consequently, an increase in transformation temperature.

In addition, microstructural refinement and increases in hardness values were observed when transformation occurred from a deformed austenite (finer microstructure in Cycle B and Cycle C than in Cycle A), mainly at the lowest cooling rates of 5, 10, and 20 °C/s. A higher accumulation of deformation in the austenite prior to transformation encourages the increase in ferrite nucleation sites and ensures the formation of finer microstructures. Similar characteristics for CCT diagrams of HSLA steels are also reported in literature [22].

3.2. Microstructural Evolution Predictions Using Microsim-SM[®]

The MicroSim-SM[®] Steckel mill model allows the evolution of austenite conditioning to be predicted and can be a very useful tool in designing the optimum combination of rolling schedule and alloy composition [38,46]. In the present study, MicroSim-SM[®] v1.0

software was used to predict the microstructural evolution of austenite in terms of average values and homogeneity during Steckel hot rolling simulation. This analysis supports the understanding of the mechanisms involved and the interaction between precipitation and recrystallization in each alloy composition. MicroSim-SM[®] requires the initial austenite grain size distribution as an input and outputs the size distribution for recrystallized and unrecrystallized fractions at the onset of subsequent rolling passes. For such purpose, the model assumes the interaction between different mechanisms acting during the interpass time, such as static and metadynamic recrystallization, grain growth, and Nb (C,N) strain-induced precipitation. The equations implemented in the model were developed from industrially produced sheets for plain CMn and microalloyed grades with Nb, Ti, and/or Mo, and adapted for a wide range of initial austenite grain sizes and rolling conditions [38].

In this study, different rolling strategies were evaluated, varying the percentual thickness reductions in each pass, both in the roughing and finishing stages. The main result that reflects microstructural refinement in the final product is the austenitic grain size throughout rolling and the value observed in the last rolling pass, before austenite decomposition. The lower the average value observed in this step (last pass), the lower the average value in the final product [55].

Figure 4a–d show the results of the optimized simulation, i.e., the one that evidenced the best conditions for maximum microstructural refinement at the end of rolling. The evolution of the average austenitic grain size and the $D_{c0.1}$ value throughout rolling is shown in Figure 4a, with the $D_{c0.1}$ parameter corresponding to grain size relative to 10% of the coarsest grains in the tail of the distribution, and this can be considered as a way of measuring the degree of heterogeneity [56].

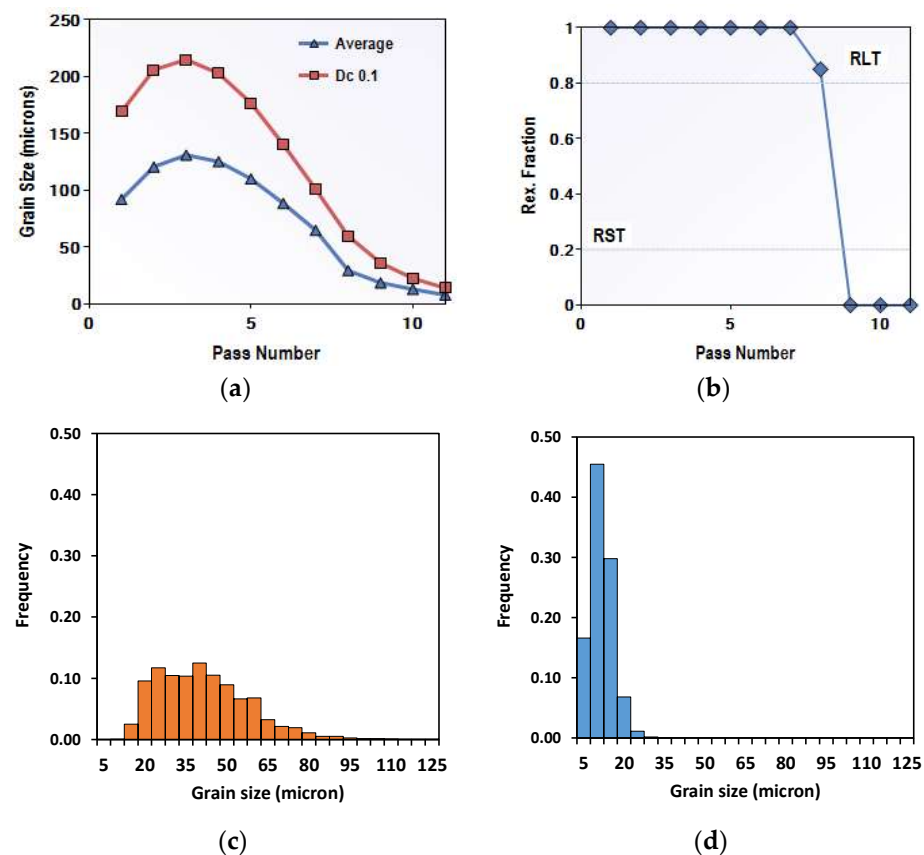


Figure 4. Microstructural evolution predictions using MicroSim-SM[®] for: (a) average austenite grain size and $D_{c0.1}$ values; (b) recrystallized fraction evolution; (c) austenite grain size distribution at the end of roughing; (d) austenite grain size distribution at the end of finishing.

Optimized rolling conditions indicate rolling with 11 deformation passes. The average austenitic grain size at the end of rolling was 8 μm , with a $D_{C0.1}$ value of 14.1 μm and maximum austenitic grain size of 35 μm , as shown in Figure 4a. This level of refinement is a consequence of the high percentage of reduction observed in roughing passes (passes 1 to 8), where the rolling temperature is above the non-recrystallization temperature, which represents the best strategy for a high level of microstructural refinement at the end of rolling [55]. Figure 4b shows the evolution of recrystallized fraction during the rolling sequence, while Figure 4c and d show the grain size distribution at the end of roughing and at the end of finishing passes, respectively.

The non-recrystallization temperature of 992 $^{\circ}\text{C}$ reported in Figure 2b was selected as the one to set as the industrial reference for the roughing-to-finishing transition. The reduction percentage applied above T_{nr} (roughing passes) was 80.5%, and the recrystallization process was complete after each applied pass within this temperature change. The microstructural refinement in this phase derives from the solute drag mechanism. A total reduction of 73.2% was observed in the case of the region below the experimentally defined T_{nr} , while reductions applied at temperatures below T_{nr} resulted in a more refined final microstructure, deriving from the pancake austenitic structure [57]. According to the simulation results obtained, the last three rolling passes (finishing passes) must be performed below T_{nr} , and these were the best conditions verified among those evaluated in the thermomechanical simulator.

Mean Flow Stress (MFS) analysis shown in Figure 5 shows the MicroSim-SM[®] plot for validation of model predictions. In this chart, the comparison is plotted between the Mechanical MFS, calculated using rolling mill load data [58], and MicroSim model predictions based on the metallurgical calculations of flow stress using a modified model, according to the method proposed by Misaka [59,60]. The sharp change in slope between the roughing and finishing passes clearly reflects the strain accumulation during the last passes. The agreement in terms of MFS calculations using both methods validates the microstructural model predictions in this case.

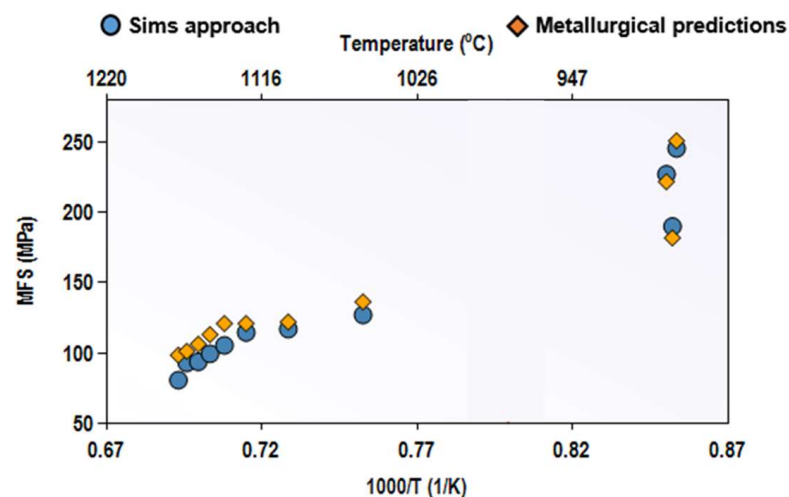


Figure 5. Mean Flow Stress (MFS) calculations and MicroSim-SM[®] predictions for optimized rolling sequence. Blue dots refer to MFS calculations based on rolling mill loads (Sims model) while yellow dots are the MFS metallurgical predictions based on Misaka-type models.

3.3. Mechanical and Microstructural Characterization of Hot-Rolled Products

The physical and computational simulations provided the rolling process parameters for the production of strips in the Steckel rolling mill. In order to evaluate the impact of coiling temperature in terms of the contribution to precipitation, four different scenarios were proposed: 525–550 $^{\circ}\text{C}$ /550–600 $^{\circ}\text{C}$ /600–650 $^{\circ}\text{C}$ /650–700 $^{\circ}\text{C}$.

Table 2 shows the results of mechanical properties obtained in the tensile test. The highest values obtained were associated with coiling temperatures of 600–650 °C, and yield strength values of 586, 605, 657, and 586 MPa were measured for coiling temperatures of 525–550 °C/550–600 °C/600–650 °C/650–700 °C, respectively. There is a narrow range of coiling temperatures that maximize the precipitation of TiC during and/or after this stage, allowing for an increase in properties. This temperature range was identified as being between 600 °C and 650 °C in continuous rolling mills [61], and similar behavior was observed in this study, in which the production process was carried out in a Steckel reversible rolling mill.

Table 2. Mechanical properties obtained from tensile test.

Sample	Coiling Temperature (°C)	Yield Strength (MPa)	Tensile Strength (MPa)	Elongation (%)
1	500–550	586 ± 4.4	666 ± 1.5	20 ± 1.0
2	550–600	605 ± 1.5	685 ± 4.6	24 ± 1.5
3	600–650	657 ± 6.5	740 ± 4.0	21 ± 0.4
4	650–700	586 ± 2.9	675 ± 4.0	21 ± 1.0

Representative samples of the four coiling conditions were taken for the purpose of microstructural analysis, and EBSD scans were performed in the center and quarter position of the thickness in order to quantify different microstructural parameters such as unit size distribution. In addition, hardening due to dislocation density was evaluated from the Kernel Average Misorientation obtained in EBSD results. For their part, different imaging options, such as Grain Boundary and Kernel maps, were analyzed and crystallographic unit sizes measured in accordance with different misorientation criteria. The microstructural characterization methodology by EBSD has been successfully applied when the objective is to understand the most active strengthening mechanisms in thermomechanically rolled products [6].

Figure 6a–d show grain boundary maps obtained through SEM-EBSD analysis for the entire range of coiling temperatures. Low and high angle boundaries were drawn, represented in red and black, while the boundaries located between $4^\circ < \vartheta < 15^\circ$ (in red) and $\vartheta > 15^\circ$ (in black) were considered as low and high angle boundaries, respectively. Low-angle-misorientation grains are assumed to contribute to strength properties due to their opposition to dislocation movement, whilst high angle boundaries are considered effective in controlling crack propagation [6]. In all cases, fine microstructures were observed, taking both misorientation criteria into consideration. When considering low-angle-misorientation criteria, mean grain sizes varied between 2.7 µm (for coiling temperature of 550–600 °C) and 3.4 µm (coiling temperature of 500–550 °C), while values ranged between 3.2 µm and 4.1 µm in the case of high angle boundaries.

Figure 7a,b show the grain size distribution corresponding to Sample 2 (coiling temperature of 550–600 °C), taking low-angle-misorientation criteria and both center and quarter positions through thickness into consideration. A similar unit size distribution was quantified for both locations, reflecting the formation of a homogeneous microstructure through thickness. The same analysis could be extended to the other specimens by also comparing samples taken from the central region and closer to the sample surfaces. Figure 8a,b show the grain size distribution corresponding to the center and quarter, both misorientation threshold criteria, and all coiling temperatures. No significant differences were noted at different locations along the thickness and a similar grain size distribution was measured for the different coiling temperatures. Therefore, the differences detected in tensile properties cannot only be explained by the strengthening mechanism related to unit size refinement. Furthermore, coiling temperature had no significant influence on the grain size distribution of the rolled products.

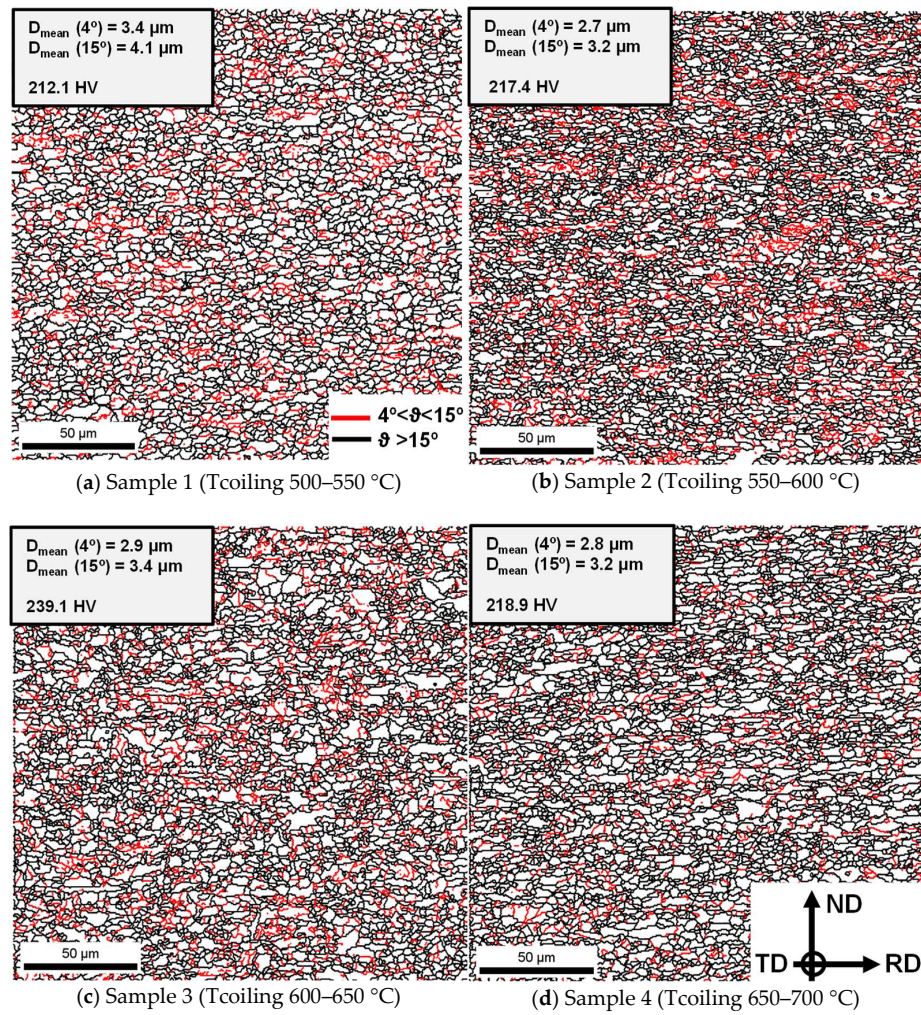


Figure 6. Image of the microstructure obtained via SEM-EBSD (grain boundary maps). Different coiling temperatures: (a) 525–550 °C; (b) 550–600 °C; (c) 600–650 °C; (d) 650–700 °C.

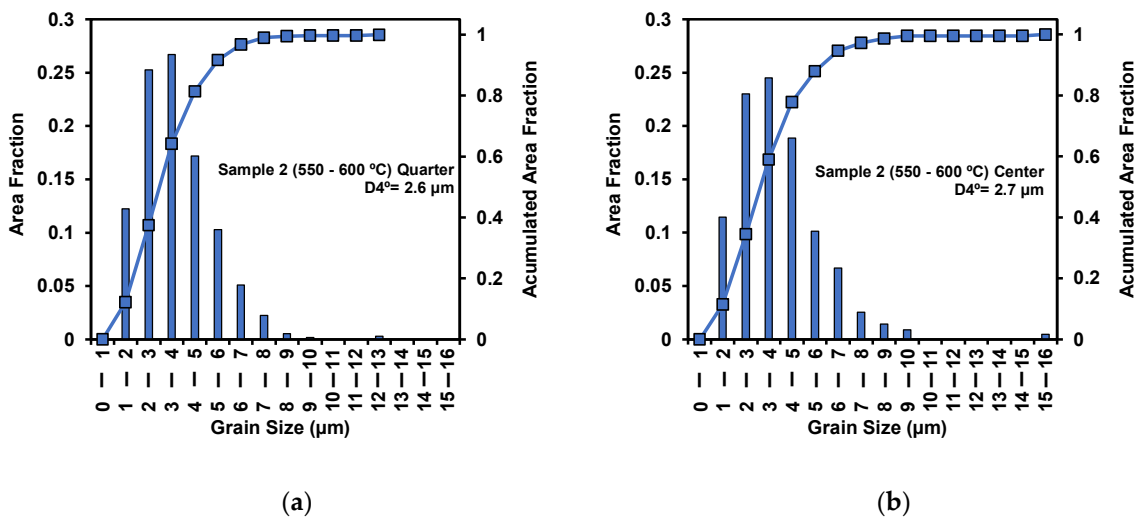


Figure 7. Grain size distribution obtained in Sample 2 (coiling temperature of 550–600 °C) at different locations along the thickness: (a) quarter and (b) center of the thickness.

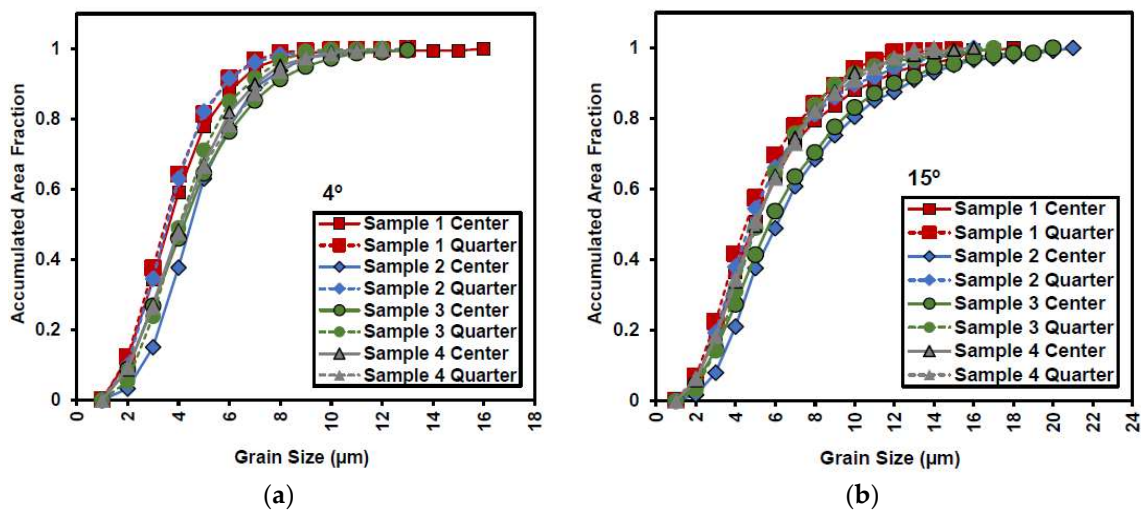


Figure 8. Comparison between the grain size distribution obtained in the different samples and both positions of thickness (quarter and center): (a) low-angle- and (b) high-angle-misorientation criteria.

The presence of Nb in HSLA steel produced in a thermomechanical process encourages austenite conditioning during deformation. Niobium interferes considerably in recrystallization kinetics in hot rolling, as its presence delays the recovery and recrystallization processes of austenite, in addition to inhibiting the growth of recrystallized grains. As a result, the formation of fine ferritic grains occurs after phase transformation. Nb contents higher than 0.05 wt% are enough to anchor the recrystallization fronts, leading to “pancaking” (elongated grains) of the austenitic microstructure and the formation of deformation bands and subgrains. Additionally, Nb also provides precipitation hardening. A similar effect can be attributed to the presence of titanium, which, at contents close to 0.1 wt%, also retards austenite recrystallization kinetics of HSLA steels, albeit in this case due to the formation of TiN and TiC [62–64].

Hardening due to dislocation density has to be considered, and the Kernel Average Misorientation measured by EBSD was estimated for such purpose. The Kernel maps obtained at each coiling temperature can be compared in Figure 9, and it can be observed that Sample 4 (coiling temperature of 650–700 °C) showed a slightly lower Kernel Average Misorientation value in both locations, confirming the formation of a more ferritic microstructure with slightly lower dislocation density. However, no significant differences were observed among the microstructures analyzed.

The yield strength of low-carbon microalloyed steels can be described as a combination of different strengthening contributions [65–67]. Although the most widely used approach is based on a linear summation of such contributions [63,68,69], several non-linear relationships, which consider the interaction of different strengthening mechanisms, have also been reported in the literature [70,71]. In the present study, a linear approach based on the sum of contributions (solid solution [40], grain size [41], dislocations [42], and fine precipitation [32]) was the one considered (see Equation (2)). To estimate individual contributions, equations previously reported in the literature were employed and are listed in Equations (3) to (6), while a more detailed description of the expressions can be found in [26]. For estimating the contribution of grain size refinement, low-angle-misorientation unit sizes were assumed. It is widely known that low angle boundaries (4°) provide an effective barrier to dislocation movement, controlling the tensile properties. Nevertheless, the high-angle-misorientation unit sizes are considered effective at controlling crack propagation and are related to toughness properties. The contribution of fine precipitation (σ_{ppt}) was estimated for the purpose of this study by subtracting the strengthening associated with all other contributions from the experimental yield strength, due to the lack of any accurate measurement of precipitate volume fraction.

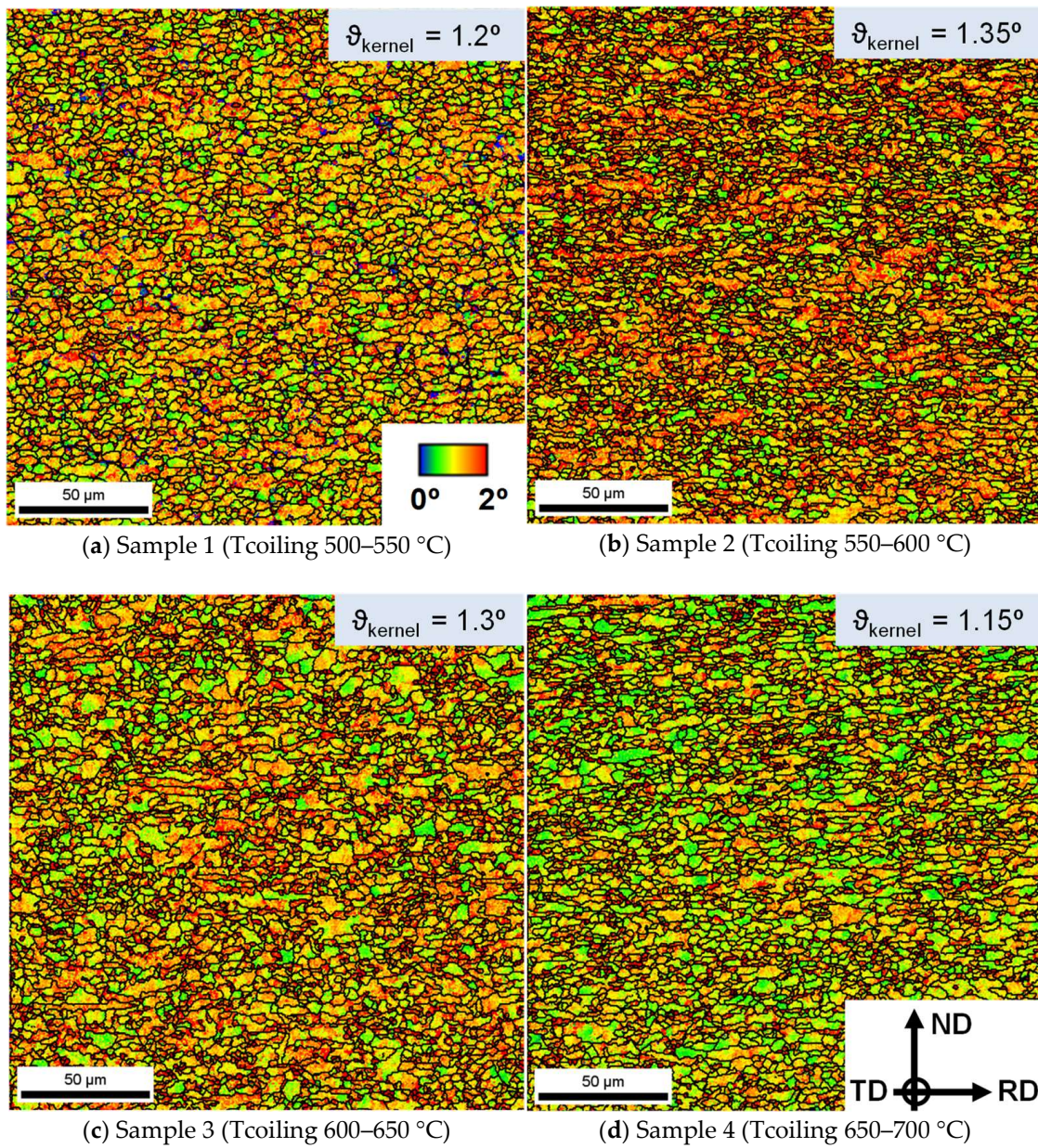


Figure 9. Kernel maps corresponding to the different coiling temperatures: (a) Sample 1 (Tcoiling 500–550 °C), (b) Sample 2 (Tcoiling 550–600 °C), (c) Sample 3 (Tcoiling 600–650 °C), (d) Sample 4 (Tcoiling 650–700 °C).

$$\text{General: } \sigma_y = \sigma_0 + \sigma_{ss} + \sigma_{gs} + \sigma_\rho + \sigma_{MA} + \sigma_{ppt} \quad (2)$$

$$\text{Solid solution: } \sigma_{ss} = \sigma_0 + 32.3Mn + 83.2Si + 11Mo + 354(\%N_{free})^{0.5} \quad (3)$$

$$\text{Grain size: } \sigma_{gs} = 17.4D_4^{-0.5} \quad (4)$$

$$\text{Dislocations: } \sigma_\rho = \alpha M \mu b \sqrt{\rho}, \text{ where } \rho = \frac{2\vartheta}{ub} \quad (5)$$

$$\text{Precipitation: } \sigma_{ppt} = 10.8 \frac{f_v^{0.5}}{x} \ln\left(\frac{x}{6.125 \cdot 10^{-4}}\right) \quad (6)$$

The results shown in Figure 10 indicate that the most relevant contribution was associated with unit size refinement and its value varied from 313 (600–650 °C) to 341 MPa (550–600 °C). No considerable difference in strengthening due to dislocation density was identified in the different samples (72 MPa in the case of Sample 4 and 77 MPa in those of the rest of the coils). As for hardening due to fine precipitation, it was observed that the highest contribution was obtained in Sample 3 (161 MPa) in which a coiling temperature range of 600–650 °C was applied. In the case of Samples 1, 2, and 4, lower precipitation hardening was quantified of 81, 68, and 79 MPa, respectively. Therefore, the highest yield strength of 657 MPa reached in Sample 3 can be justified by the formation of fine and abundant precipitation.

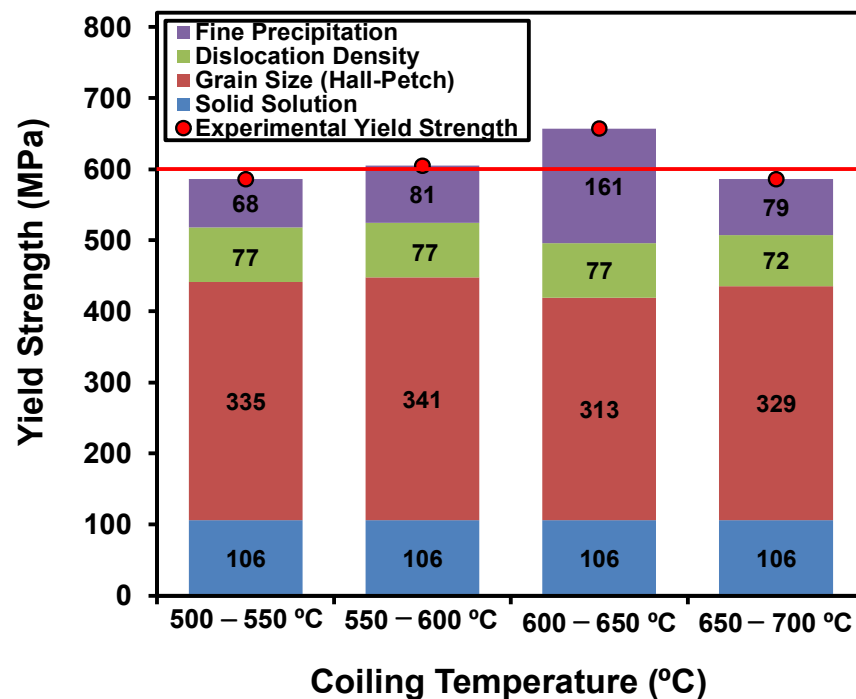


Figure 10. Contributions of different strengthening mechanisms to material yield strength.

Samples 2, 3, and 4 were selected to analyze fine precipitation in the transmission electron microscope (TEM). TEM micrographs corresponding to Sample 3 (coiling temperature of 600–650 °C) are shown in Figure 11, in which different precipitate populations can be distinguished deriving from different steps in the process. The coarsest precipitates (coarser than 30 nm) are usually associated with the lack of complete dissolution of Nb-rich particles during initial soaking. Precipitates ranging between 10 and 20 nm can be related to the strain-induced precipitation taking place in the austenite during finishing deformation passes (below T_{nr}). In addition, in Sample 3, very fine precipitates smaller below 10 nm were also detected, and these, which formed during cooling (run-out table or coiling), are effective in encouraging a hardening effect. The microanalysis performed in the different types of precipitates suggest that they were mainly Nb- and Ti-rich ones (see an example in Figure 11d).

The presence of TiC can be evidenced in all samples analyzed, albeit with a higher fraction in the sample submitted at the coiling temperature of 600–650 °C, as can be observed in Figure 12, which provides a comparison between the three samples analyzed. In Sample 3, a higher fraction of fine precipitates was observed compared to Sample 2 and Sample 4.

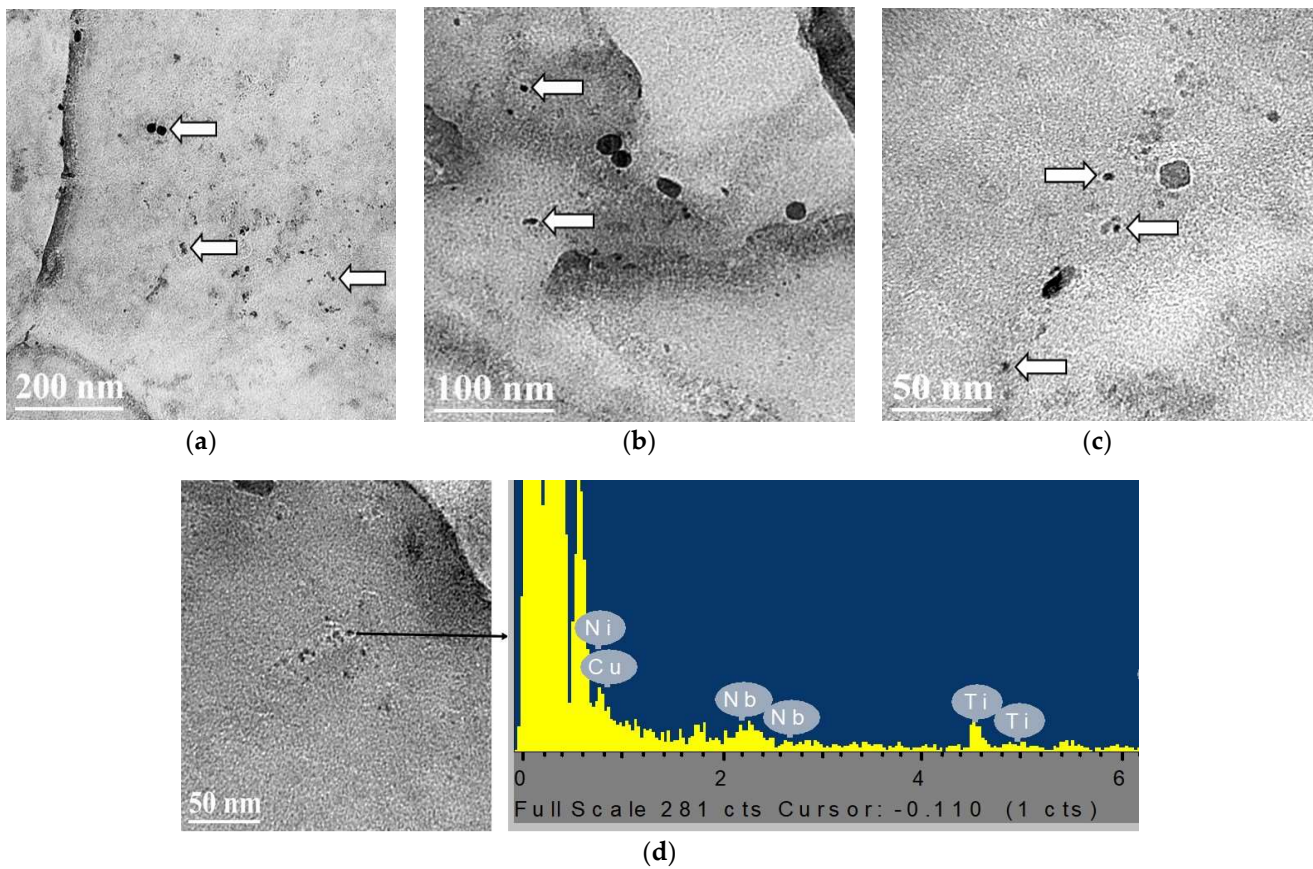


Figure 11. (a–c) TEM micrographs illustrating the presence of fine Ti carbides in Sample 3 (600–650 °C) (precipitates are indicated in arrows). (d) Microanalysis of a Nb-Ti rich precipitate.

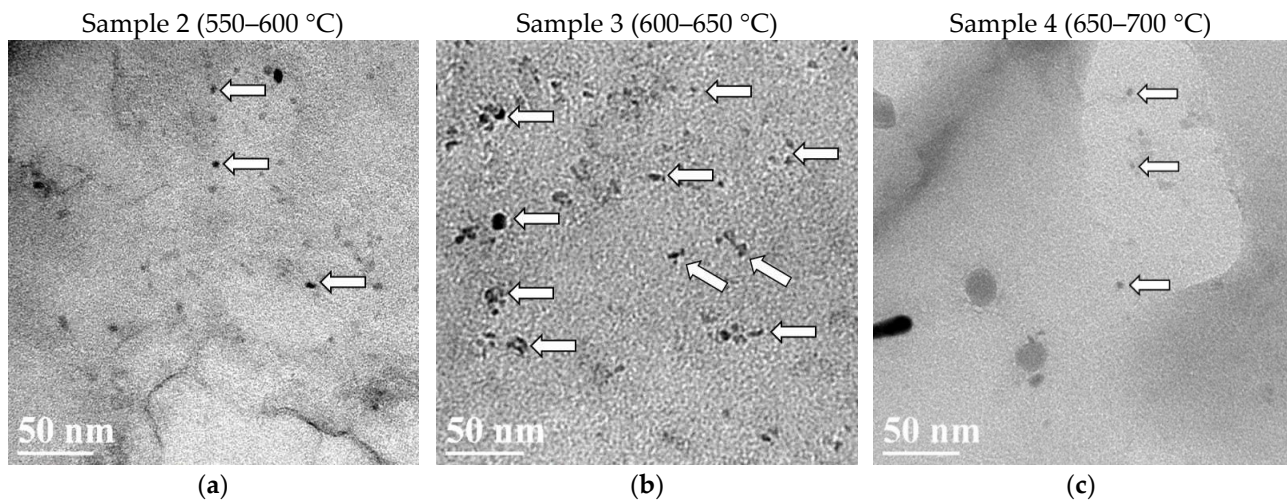


Figure 12. Effect of coiling temperature on TiC precipitation (precipitates are indicated in arrows): (a) Sample 2 (Tcoiling 550–600 °C), (b) Sample 3 (Tcoiling 600–650 °C), (c) Sample 4 (Tcoiling 650–700 °C).

Precipitates below 10 nm contribute to the increase in mechanical properties, as they are the most effective in anchoring dislocations [30]. Table 3 shows the precipitate average diameters for each evaluated coiling temperature, and Sample 3 provided an average particle size of 3.9 nm, while Sample 2 (5 nm) and Sample 4 (6.3 nm) evidenced higher

precipitate diameter values. The value obtained for coils within a coiling temperature range of 600–650 °C was 22% lower than that found at a temperature range of 550–600 °C and 38% lower than that observed at a temperature of 650–700 °C. Figure 13 shows the distribution of precipitates below 10 nm. It can be verified that Sample 3, referring to a coiling temperature of 600–650 °C, had a normal distribution with a peak around 3 nm, showing that under this condition, the precipitates were finer than in the others, thus justifying the higher yield strength observed.

Table 3. Mean precipitate diameters for the different coiling temperatures.

	Coiling Temperature (°C)	Precipitate Diameter (nm)
Sample 2	550–600	5.0 ± 0.1
Sample 3	600–650	3.9 ± 0.2
Sample 4	650–700	6.3 ± 0.3

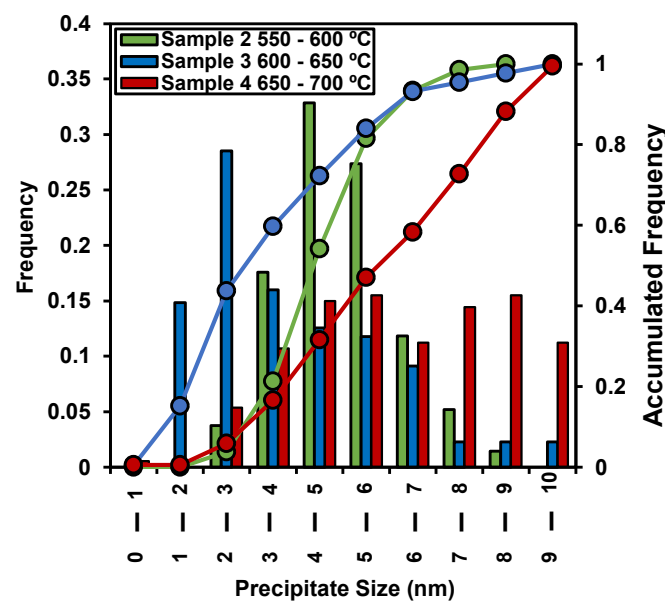


Figure 13. Effect of coiling temperature on precipitate size distribution (below 10 nm).

Regarding estimation of the contribution of the different hardening mechanisms shown in Figure 10, the value assigned to precipitation was corroborated by precipitate analysis. It was evidenced that reaching a yield strength above 600 MPa in this alloy is associated with strict coiling temperature control, while the use of non-stoichiometric titanium was another relevant point in the development of this work.

According to the Ashby–Orowan model (Equation (6)), an increase in 30 MPa in precipitation strengthening could be obtained in the case of a constant precipitate volume fraction of 0.001 involving reducing the precipitate size from 6 nm to 4 nm, as shown in Figure 14. One of the greatest limitations in evaluating the contribution of precipitation hardening is how to obtain an accurate calculation of the precipitate volume fraction, but although this cannot be accurately quantified, it could be stated that small differences in precipitate size might exert relevant differences in terms of their hardening effect.

Based on Equation (6) and considering the estimated hardening due to fine precipitation together with the previously measured precipitate sizes, the corresponding precipitate volume fraction could then be calculated. In the case of Sample 1, a precipitate volume fraction of $f_v = 0.00025$ was estimated, $f_v = 0.00039$ in that of Sample 4, and $f_v = 0.00124$ in that of Sample 3. These volume fractions are within the range previously reported in the literature for similar chemistries. According to Thermocalc calculations, the equilibrium precipitate volume fraction was about 0.0013 (estimated f_v values are below this value).

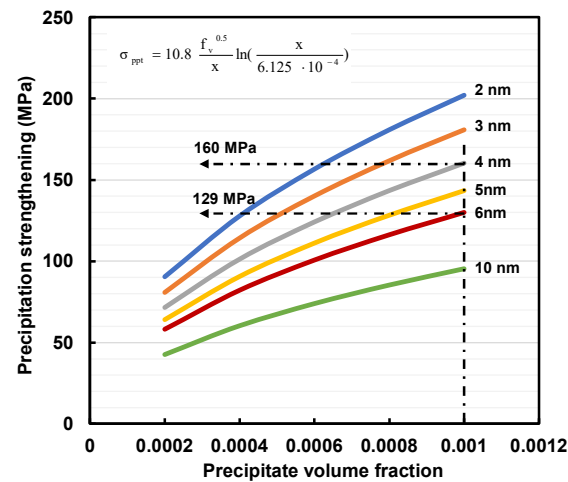


Figure 14. Contribution of precipitate size to precipitation strengthening according to the Ashby–Orowan model.

4. Conclusions

The combination of advanced modeling techniques with the industrial know-how in defining optimum rolling strategies provided an interesting approach to obtaining the mechanical properties requested in high-strength coils of non-stoichiometric Nb-Ti HSLA steel. Furthermore, the application of systematic characterization techniques helps understand the metallurgical mechanisms behind strengthening contributions, thus supporting further improvements in alloy design/processing route optimization.

In this study, the industrially hot-rolled product showed a high level of microstructural refinement, with average values of ferritic grain size within the range of 2.4 μm to 3 μm , and good homogeneity was also observed along the thickness in all samples analyzed. The results show that, despite the long rolling times typical of the Steckel reversing mill, the addition of niobium and non-stoichiometric titanium constituted a suitable approach to obtaining refined and homogeneous microstructure in the final product.

Coiling temperature had no impact on dislocation hardening and grain size hardening mechanisms. However, there was a major influence on precipitation hardening. For their part, yield strength values above 650 MPa and tensile strength values above 700 MPa were obtained for rolled strips within a coiling temperature range of 600–650 $^{\circ}\text{C}$. Analysis of TiC precipitates via transmission electron microscopy showed that this temperature range potentialized precipitation hardening, thus encouraging a greater volume of fine precipitates, which was maximized by the presence of non-stoichiometric titanium. As a result, the yield strength observed was 50 MPa above that obtained within the coiling temperature range of 550–600 $^{\circ}\text{C}$ and 70 MPa above ranges of 525–550 $^{\circ}\text{C}$ and 650–700 $^{\circ}\text{C}$.

Author Contributions: Conceptualization, C.A.M. and G.L.d.F.; methodology, C.A.M., G.L.d.F., J.A.C.C. and A.L.d.S.; software, A.A.G. and P.U.; validation, U.M., N.I., C.A.M., G.L.d.F. and P.U.; formal analysis, G.L.d.F. and P.U.; investigation, U.M., N.I., C.A.M. and G.L.d.F.; resources, C.A.M., G.L.d.F., J.A.C.C. and A.L.d.S.; writing—original draft preparation, C.A.M.; writing—review and editing, all; supervision, G.L.d.F., J.M.R.-I. and P.U.; project administration, C.A.M., M.A.R. and J.M.R.-I.; funding acquisition, J.M.R.-I. and M.A.R. All authors have read and agreed to the published version of the manuscript.

Funding: This research was partially funded by CBMM—Companhia Brasileira de Mineração e Metalurgia.

Institutional Review Board Statement: Not applicable.

Informed Consent Statement: Not applicable.

Data Availability Statement: Not applicable.

Acknowledgments: The authors wish to thank Gerdauro Ouro Branco, CBMM—Companhia Brasileira de Mineração e Metalurgia, and Universidade Federal de Ouro Preto for all the support provided throughout the development of this work.

Conflicts of Interest: The authors declare no conflict of interest.

Nomenclature

σ_y	Yield Strength
σ_0	Lattice friction stress
σ_{ss}	Strengthening contribution due to solid solution
σ_{gs}	Strengthening contribution due to grain size
σ_ρ	Strengthening contribution due to dislocations
σ_{ppt}	Strengthening contribution due to precipitation
A	Numerical factor
M	Taylor factor
μ	Shear modulus
b	Burgers vector magnitude
ρ	Dislocation density
ϑ	Kernel average misorientation
u	Unit length related to Kernel
f_v	Volume fraction of precipitates
x	Radius of precipitates

References

1. Ghosh, M.; Bart, K.; Das, S.K.; Kumar, B.R.; Pramanick, A.K.; Chakraborty, J.; Das, G.; Hadas, S.; Bharathy, S.; Ray, S.K. Variation in mechanical properties and heterogeneity in microstructure of high-strength ferritic steel during mill trial. *Metall. Mater. Trans. A* **2014**, *45*, 2719–2731. [[CrossRef](#)]
2. Kim, Y.W.; Song, S.W.; Seo, S.J.; Hong, S.G.; Lee, C.S. Development of Ti and Mo micro-alloyed hot-rolled high strength sheet steel by controlling thermomechanical controlled processing schedule. *Mater. Sci. Eng. A* **2013**, *565*, 430–438. [[CrossRef](#)]
3. Mao, X.; Huo, X.; Sun, X.; Chai, Y. Strengthening mechanisms of a new 700 MPa hot rolled Ti-microalloyed steel produced by compact strip production. *Mater. Process. Technol.* **2010**, *210*, 1660–1666. [[CrossRef](#)]
4. García-Sesma, L.; López, B.; Pereda, B. Effect of coiling conditions on the strengthening mechanisms of Nb microalloyed steels with high Ti addition levels. *Mater. Sci. Eng. A* **2019**, *748*, 386–395. [[CrossRef](#)]
5. Iza-Mendia, A.; Altuna, M.A.; Pereda, B.; Gutierrez, I. Precipitation of Nb in ferrite after austenite conditioning. Part I: Microstructural characterization. *Metall. Mater. Trans. A* **2012**, *43*, 4553–4570. [[CrossRef](#)]
6. Isasti, N.; Jorge-Badiola, D.; Taheri, M.L.; Uranga, P. Microstructural and Precipitation Characterization in Nb-Mo Microalloyed Steels: Estimation of the Contributions to the Strength. *Metall. Mater. Int.* **2014**, *20*, 807–817. [[CrossRef](#)]
7. Medina, S.F.; Chapa, M.; Valles, P.; Quispe, A.; Vega, M.I. Influence of Ti and N contents on austenite grain control and precipitate size in structural steels. *ISIJ Int.* **1999**, *39*, 930–936. [[CrossRef](#)]
8. Lagneborg, R.; Siwecki, T.; Zajac, S.; Hutchinson, B. Role of vanadium in microalloyed steels. *Scand. J. Metall.* **1999**, *28*, 186–241.
9. Freeman, S.; Honeycombe, R.W.K. Strengthening of titanium steels by carbide precipitation. *Met. Sci.* **1977**, *11*, 59–64. [[CrossRef](#)]
10. Uemori, R.; Chijiwa, R.; Tamehiro, H.; Morikawa, H. AP-FIM study on the effect of Mo addition on microstructure in Ti-Nb steel. *Appl. Surf. Sci.* **1994**, *76–77*, 255–260. [[CrossRef](#)]
11. Honeycombe, R.W.K.; Mehl, R.F. Transformation from austenite in alloy steels. *Metall. Mater. Trans.* **1976**, *7*, 915–936. [[CrossRef](#)]
12. Chen, C.; Yang, J.; Chen, C.; Cheng, S. Microstructural characterization and strengthening behavior of nanometer sized carbides in Ti-Mo microalloyed steels during continuous cooling process. *Mater. Character.* **2017**, *114*, 18–19. [[CrossRef](#)]
13. Timokhina, I.; Miller, M.K.; Wang, J.; Beladi, H.; Cizek, P.; Hodgson, P.D. On the Ti-Mo-Fe-C atomic clustering during interphase precipitation in the Ti-Mo steel studied by advanced microscopic techniques. *Mater. Des.* **2016**, *111*, 222–229. [[CrossRef](#)]
14. Chen, J.; Wang, G. Precipitation Characteristics in a Low-Carbon Vanadium–Titanium-Bearing Steel. *Steel Res.* **2015**, *86*, 821–824. [[CrossRef](#)]
15. Challa, V.S.A.; Zhou, W.H.; Misra, R.D.K.; O'Malley, R.; Jansto, S.G. The effect of coiling temperature on the microstructure and mechanical properties of a niobium–titanium microalloyed steel processed via thin slab casting. *Mater. Sci. Eng. A* **2014**, *595*, 143–153. [[CrossRef](#)]
16. Bu, F.Z.; Wang, X.M.; Yang, S.W.; Shang, J.; Misra, R.D.K. Contribution of interphase precipitation on yield strength in thermomechanically simulated Ti–Nb and Ti–Nb–Mo microalloyed steels. *Mater. Sci. Eng. A* **2015**, *620*, 22–29. [[CrossRef](#)]
17. Sesma, L.G.; López, B.; Pereda, B. Effect of Deformation Sequence and Coiling Conditions on Precipitation Strengthening in High Ti–Nb–Microalloyed Steels. *Metall. Mater. Trans. A* **2022**, *53*, 2270–2285. [[CrossRef](#)]

18. Chen, C.Y.; Yen, H.W.; Kao, F.H.; Li, W.C.; Huang, C.Y.; Yang, J.R.; Wang, S.H. Precipitation hardening of high-strength low-alloy steels by nanometer-sized carbides. *Mater. Sci. Eng. A* **2009**, *499*, 162–166. [[CrossRef](#)]
19. Wang, Z.; Zhang, H.; Guo, C.; Liu, W.; Yang, Z.; Sun, X.; Zhang, Z.; Jiang, F. Effect of molybdenum addition on the precipitation of carbides in the austenite matrix of titanium micro-alloyed steels. *Mater. Sci.* **2016**, *51*, 4996–5007. [[CrossRef](#)]
20. Gan, X.; Yuan, Q.; Zhao, G.; Ma, H.; Liang, W.; Xue, Z.; Qiao, W.; Xu, G. Quantitative Analysis of Microstructures and Strength of Nb-Ti Microalloyed Steel with Different Ti Additions. *Metall. Mater. Trans. A* **2020**, *51*, 2084–2096. [[CrossRef](#)]
21. Bruna, R.; Ebril, G.; Cerliani, A.; Moriconi, J.; Garcia, C.I. A cost-effective approach to the development of high-strength-high-toughness NbVTi-based HSLA steels for the agricultural and heavy transportation industries. *Iron Steel Technol.* **2018**, *15*, 66–72.
22. Isasti, N.; Jorge-Badiola, D.; Taheri, M.L.; Beatriz, L.; Uranga, P. Effect of Composition and Deformation on Coarse-Grained Austenite Transformation in Nb-Mo Microalloyed Steels. *Metall. Mater. Trans. A* **2011**, *42*, 3729–3742. [[CrossRef](#)]
23. Mao, X.P. *Microalloying Technology on Thin Slab Casting and Direct Rolling Process*; Metal Industry Press: Beijing, China, 2008.
24. Isasti, N.; Jorge-Badiola, D.; Taheri, M.L.; Uranga, P. Microstructural Features Controlling Mechanical Properties in Nb-Mo Microalloyed Steels. Part I: Yield Strength. *Metall. Mater. Trans. A* **2014**, *45*, 4960–4971. [[CrossRef](#)]
25. Misra, R.D.K.; Nathani, H.; Hartmann, J.E.; Siciliano, F. Microstructural evolution in a new 770 MPa hot rolled Nb–Ti microalloyed steel. *Mater. Sci. Eng. A* **2005**, *394*, 339–352. [[CrossRef](#)]
26. Altuna, M.A.; Iza-Mendia, A.; Gutierrez, I. Precipitation of Nb in Ferrite After Austenite Conditioning. Part II: Strengthening Contribution in High-Strength Low-Alloy (HSLA) Steels. *Metall. Mater. Trans. A* **2012**, *43*, 4571–4586. [[CrossRef](#)]
27. Kim, Y.W.; Kim, J.H.; Hong, S.G.; Lee, C.S. Effects of rolling temperature on the microstructure and mechanical properties of Ti–Mo microalloyed hot-rolled high strength steel. *Mater. Sci. Eng. A* **2014**, *605*, 244–252. [[CrossRef](#)]
28. Yang, G.W.; Sun, X.J.; Yong, Q.L.; Li, Z.D.; Li, X.X. Austenite Grain Refinement and Isothermal Growth Behavior in a Low Carbon Vanadium Microalloyed Steel. *J. Iron Steel Res. Int.* **2014**, *21*, 757–764. [[CrossRef](#)]
29. Yang, G.W.; Sun, X.J.; Li, Z.D.; Li, X.X.; Yong, Q.L. Effects of vanadium on the microstructure and mechanical properties of a high strength low alloy martensite steel. *Mater. Des.* **2013**, *50*, 102–107. [[CrossRef](#)]
30. Larzabal, G.; Isasti, N.; Rodriguez-Ibabe, J.M.; Uranga, P. Evaluating strengthening and impact toughness mechanisms for ferritic and bainitic microstructures in Nb, Nb-Mo and Ti-Mo microalloyed steels. *Metals* **2017**, *7*, 65. [[CrossRef](#)]
31. Xu, G.; Gan, X.L.; Ma, G.J.; Luo, F.; Zou, H. The development of Ti-alloyed high strength microalloy steel. *Mater. Des.* **2010**, *31*, 2891–2896. [[CrossRef](#)]
32. Gladman, T. Precipitation hardening in metals. *Met. Sci. J.* **1999**, *15*, 30–36. [[CrossRef](#)]
33. Huang, H.H.; Yang, G.W.; Zhao, G.; Mao, X.P.; Gan, X.L.; Yin, Q.L.; Yi, H. Effect of Nb on the microstructure and properties of Ti-Mo microalloyed high-strength ferritic steel. *Mater. Sci. Eng. A* **2018**, *736*, 148–155. [[CrossRef](#)]
34. Zhang, K.; Li, Z.D.; Sun, X.J.; Yong, Q.L.; Yang, J.W.; Li, Y.M.; Zhao, P.L. Development of Ti–V–Mo Complex Microalloyed Hot-Rolled 900-MPa-Grade High-Strength Steel. *Acta Metall. Sin. (Eng. Lett.)* **2015**, *28*, 641–648. [[CrossRef](#)]
35. Edelman, D.G.; Wigman, S.L. Method for Producing Titanium-Bearing Microalloyed High-Strength Low-Alloy Steel. U.S. Patent n.6,669,789, 30 December 2003.
36. Baker, T.N. Titanium microalloyed steels. *Ironmak. Steelmak.* **2019**, *46*, 1–55. [[CrossRef](#)]
37. Souza, A.L.; Teixeira, L.M.; Borges, J.M.; Sales de Paula, G. Use of tension control between drum and Steckel mill to get the width of the strip in the specified tolerance. In *Utilização do Controle de Tensão Entre Dromo e Laminador Steckel para Enquadramento da Largura da Tira na Faixa Especificada, Proceedings of the 57° Seminário de Laminação e Conformação de Metais, São Paulo, SP, Brazil, 7–9 June 2022*, 6th ed.; Technical Contribution; ABM Week: São Paulo, SP, Brazil, 2002; pp. 405–416. [[CrossRef](#)]
38. Souza, A.L.; Oliveira, A.P.; Martins, C.A.; Borges, J.M.; Lino, J.J.P.; Cohn, J.A.C.; Teixeira, L.M.; Isasti, N.; Pereda, B.; Uranga, P. Microstructural Evolution during Steckel rolling and EBSD analyses of final microstructure. In *Proceedings of the 11th International Rolling Conference (IRC 2019), São Paulo, SP, Brazil, 1–3 October 2019*; pp. 599–608.
39. Pereda, B.; García-Sesma, L.; López, B. Effect of coiling temperature on the hardening mechanisms of a high-Ti steel. *Mater. Sci. Forum* **2018**, *941*, 164–169. [[CrossRef](#)]
40. Pickering, F.B.; Gladman, T. *Metallurgical Developments in Carbon Steels*; Special Report No. 81; Iron and Steel Institute: London, UK, 1963.
41. Iza-Mendia, A.; Gutiérrez, I. Generalization of the existing relations between microstructure and yield stress from ferrite–pearlite to high strength steels. *Mater. Sci. Eng. A* **2013**, *561*, 40–51. [[CrossRef](#)]
42. Kubin, L.P.; Mortensen, A. Geometrically necessary dislocations and strain-gradient plasticity: A few critical issues. *Scr. Mater.* **2003**, *48*, 119–125. [[CrossRef](#)]
43. Cardoso, R.A.; Faria, G.L. Characterization of Austenite Decomposition in Steels with Different Chemical Concepts and High Potential to Manufacture Seamed Pipes for Oil and Gas Industry. *Mater. Res.* **2019**, *22*, e20190378. [[CrossRef](#)]
44. Rodrigues, K.F.; Faria, G.L. Characterization and Prediction of Continuous Cooling Transformations in Rail Steels. *Mater. Res.* **2021**, *24*, e20200519. [[CrossRef](#)]
45. Cezário, A.L.S.; Faria, G.L. Proposition of an Empirical Functional Equation to Predict the Kinetics of Austenite to Ferrite Transformation in a Continuous Cooled IF-Ti-Stabilized Steel. *Mater. Res.* **2021**, *24*, e20200498. [[CrossRef](#)]

46. Uranga, P.; Rodriguez-Ibabe, J.M.R.; Stalheim, D.G.; Barbosa, R.; Rebellato, M. Application of practical modeling of microalloyed steels for improved metallurgy, productivity and cost reduction in hot strip mill applications. In Proceedings of the AISTech 2016 Proceedings, Pittsburgh, PA, USA, 16–19 May 2016.
47. Associação Brasileira de Normas Técnicas. *Produtos Planos de Aços—Determinação das Propriedades Mecânicas à Tração*; NBR6673; Associação Brasileira de Normas Técnicas: Sao Paulo, Brazil, 30 July 1981.
48. Wilkinson, A. A new method for determining small misorientations from electron back scatter diffraction patterns. *Scr. Mater.* **2001**, *44*, 2379–2385. [[CrossRef](#)]
49. Abad, R.; Fernández, A.I.; López, B.; Rodriguez-Ibabe, J.M. Interaction between Recrystallization and Precipitation during Multipass Rolling in a Low Carbon Niobium Microalloyed Steel. *ISIJ Int.* **2001**, *41*, 1373–1382. [[CrossRef](#)]
50. Fernandez, A.I.; López, B.; Rodriguez-Ibabe, J.M. Relationship between the austenite recrystallized fraction and the softening measured from the interrupted torsion test technique. *Scr. Mater.* **1999**, *40*, 543. [[CrossRef](#)]
51. Irvine, K.J.; Pickering, F.B.; Gladman, T. Grain refined C-Mn Steels. *J. Iron Steel Inst.* **1967**, *205*, 161–182.
52. Araki, T.; Kozasu, I.; Tankechi, H.; Shibata, K.; Enomoto, M.; Tamehiro, H. (Eds.) *Atlas for Bainitic Microstructures*; ISIJ: Tokyo, Japan, 1992; Volume 1.
53. Krauss, G.; Thompson, S.W. Ferritic Microstructures in Continuously Cooled Low- and Ultralow-carbon Steels. *ISIJ Int.* **1995**, *35*, 937–945. [[CrossRef](#)]
54. Rodriguez-Ibabe, J.M.R. *Metallurgical aspects of flat rolling process. The Making, Shaping and Treating of Steel*; Flat Products Volume; AIST: Tsukuba, Japan, 2014; Chapter 3; pp. 113–170.
55. Stalheim, D.G. Metallurgical and process strategy for the production of 700 MPa hot rolled structural steel coil. In Proceedings of the 72nd ABM Annual Congress, São Paulo, SP, Brazil, 5 October 2017; pp. 745–756.
56. Uranga, P.; Fernandez, A.I.; Lopez, B.; Rodriguez-Ibabe, J.M. Optimization of Rolling Conditions in Nb Microalloyed Steel Processed by Thin Slab Casting and Direct Rolling Route: Processing Maps. *Mater. Sci. Forum* **2005**, *500–501*, 245–252. [[CrossRef](#)]
57. Hulka, K. *Fundamentals of the controlled rolling process. Niobium Information No 7/94*; Niobium Products Company GmbH: Dusseldorf, Germany, 1994.
58. Sims, R.B. The Calculation of Roll Force and Torque in Hot Rolling Mills. *Proc. Inst. Mech. Eng.* **1954**, *168*, 191. [[CrossRef](#)]
59. Misaka, Y.; Yoshimoto, T. Formularization of mean resistance to deformation of plain carbon steels at elevated temperature. *J. Jpn. Soc. Technol. Plast.* **1967**, *8*, 414–422.
60. Minami, K.; Siciliano, F., Jr.; Maccagno, T.M.; Jonas, J.J. Mathematical Modeling of Mean Flow Stress during the Hot Strip Rolling of Nb Steels. *ISIJ Int.* **1996**, *36*, 1507–1515. [[CrossRef](#)]
61. Santos, A.A.; Murari, F.D.; Avelar Junior, A.R.; Pereda, B.; López, B.L. Evolução microestrutural de aço da classe de 700 MPa na laminação de tiras a quente. In Proceedings of the 55° Seminário de Laminação e Conformação, São Paulo, SP, Brazil, 2–4 October 2018; pp. 379–390.
62. Mao, X.; Young, Q.; Huo, X. *Titanium Microalloyed Steel: Fundamentals, Technology, and Products-Introduction*; Springer: Wuhan, China, 2016; pp. 1–32.
63. Gladman, T. *The Physical Metallurgy of Microalloyed Steels*, 2nd ed.; The Institute of Materials: London, UK, 2002.
64. Vervynck, S.; Verbeken, K.; Thibaux, P.; Houbaert, Y. Recrystallization-precipitation Interaction During Austenite Hot Deformation of a Nb Microalloyed Steel. *Mater. Sci. Eng. A* **2011**, *528*, 5519–5528. [[CrossRef](#)]
65. Charleux, M.; Poole, W.J.; Militzer, M.; Deschamps, A. Precipitation behavior and its effect on strengthening of an HSLA-Nb/Ti steel. *Metall. Mater. Trans. A* **2001**, *32*, 1635–1647. [[CrossRef](#)]
66. Carretero Olalla, V.; Bliznuk, V.; Sanchez, N.; Thibaux, P.; Kestens, L.A.I.; Petrov, R.H. Analysis of the strengthening mechanisms in pipeline steels as function of the hot rolling parameters. *Mater. Sci. Eng. A* **2014**, *604*, 46–56. [[CrossRef](#)]
67. Irvine, J.; Baker, T.N. The influence of rolling variables on the strengthening mechanisms operating in niobium steels. *Mater. Sci. Eng.* **1984**, *64*, 123–134. [[CrossRef](#)]
68. Pickering, F.B. *Physical Metallurgy and the Design of Steels*; Applied Science Publishers Ltd.: London, UK, 1978.
69. Peng, Z.; Li, L.; Gao, J.; Huo, X. Precipitation strengthening of titanium microalloyed high-strength steel plates with isothermal treatment. *Mater. Sci. Eng.* **2016**, *657*, 413–421. [[CrossRef](#)]
70. Yen, H.W.; Chen, P.Y.; Huang, C.Y.; Yang, J.R. Interphase precipitation of nanometer-sized carbides in a titanium-molybdenum-bearing low-carbon steel. *Acta Mater.* **2011**, *59*, 6264–6274. [[CrossRef](#)]
71. Yakubtsov, I.A.; Boyd, J.D.; Liu, W.J.; Essadique, E. Strengthening mechanism in dual-phase acicular ferrite+M/A microstructure. In Proceedings of the 42nd Mechanical Working and Steel Processing Conference, Iron and Steel Society/AIME, Toronto, ON, Canada, 22–25 October 2000; pp. 429–439.

Disclaimer/Publisher’s Note: The statements, opinions and data contained in all publications are solely those of the individual author(s) and contributor(s) and not of MDPI and/or the editor(s). MDPI and/or the editor(s) disclaim responsibility for any injury to people or property resulting from any ideas, methods, instructions or products referred to in the content.